Computational modelling identifies key determinants of subregion-specific dopamine dynamics in the striatum

Aske L. Ejdrup[1,†], Jakob K. Dreyer[2], Matthew D. Lycas[1], Søren H. Jørgensen[1], Trevor W. Robbins[3,4], Jeffrey W. Dalley[3,4,5], Freja Herborg[1, †, *], Ulrik Gether[1, †, *]

[1]Department of Neuroscience, Faculty of Health and Medical Sciences, Maersk Tower 7.5, University of Copenhagen, DK-2200 Copenhagen, Denmark

[2]Department of Bioinformatics, H Lundbeck A/S, Valby, Denmark

[3]Behavioural and Clinical Neuroscience Institute, University of Cambridge, Cambridge CB2 3EB, UK

[4]Department of Psychology, University of Cambridge, Cambridge CB2 3EB, UK

[5]Department of Psychiatry, University of Cambridge, Cambridge CB2 0SZ, UK

*These authors contributed equally to the work

†To whom correspondence should be addressed: ejdrup@sund.ku.dk, frejahh@sund.ku.dk or gether@sund.ku.dk

Abstract

Striatal dopamine (DA) release regulates reward-related learning and behavioural activation and is believed to consist of a short-lived *phasic* and continuous *tonic* component. Here, we build a three-dimensional model of extracellular DA dynamics in dorsal (DS) and ventral striatum (VS) that include tens of thousands of DA release sites. The model predicts rapid dynamics in DS with little-to-no basal DA, and much slower dynamics in the VS enabling build-up of a *tonic* DA level. These regional differences do not primarily reflect different release phenomena but rather arise from differential dopamine transporter (DAT) activity. Interestingly, our simulations posit prevalent nanoclustering of DAT as a possible regulator of this activity. Receptor binding simulations show that D1 receptor occupancy follows extracellular DA concentration with millisecond delay, while D2 receptors integrate DA signal over seconds. Summarized, our model distills recent experimental observations into a computational framework that challenge prevailing paradigms of striatal DA signalling.

47 ## Introduction

48 Striatal dopamine (DA) release is essential for regulating reward-related learning, incentive
49 motivation, and motor function *(Berke, 2018; Klaus et al, 2019)*. DA exerts these roles over a
50 broad range of time scales, yet DA primarily operates as a volume transmitter that targets
51 metabotropic receptors located within a micrometre range from the sites of release *(Agnati*
52 *et al, 1995; Borroto-Escuela et al, 2018; Cragg & Rice, 2004; Gonon et al, 2000; Sulzer et al,*
53 *2016)*. The temporal and spatial dynamics of DA release in striatum, however, remain a
54 highly contested topic. Classically, DA release has been divided into *tonic* release, driven by
55 pacemaker-like spontaneous firing, and *phasic* release from coordinated bursts of firing
56 across neurons *(Niv et al, 2007; Schultz, 2007; Sulzer et al., 2016)*. However, this sharp
57 distinction in release modes, as well as the existence of a basal DA level has recently been
58 challenged *(Berke, 2018; Ejdrup et al, 2023; Jorgensen et al, 2023; Liu et al, 2021; Sippy &*
59 *Tritsch, 2023)*.

60 The picture is further complicated by major regional differences across striatal sub
61 domains. These include differences in Ca^{2+}-channel and nicotinic acetylcholine receptor
62 (nAChR) expression profiles on DA terminals, as well differential regulation and expression
63 of the DA transporter (DAT) *(Brown et al, 2011; Cardozo & Bean, 1995; Kearney et al, 2023;*
64 *Richards & Zahniser, 2009; Threlfell et al, 2010)*. In addition, we and others have found
65 remarkable differences in extracellular DA release dynamics between the dorsal (DS) and
66 ventral striatum (VS) *(Jorgensen et al., 2023; Mohebi et al, 2024; Salinas et al, 2023)*. Fibre
67 photometry recordings in the DS in mice using the DA sensor dLight1.3b during self-paced
68 exploratory activity showed a rapidly fluctuating signal, whereas we observed up to
69 minutes-long DA dynamics in VS that correlated with behavioural output *(Jorgensen et al.,*

70 *2023)*. Concurrent measurements of extracellular DA by microdialysis and fibre photometry
71 have furthermore corroborated the lack of tonic levels of DA in DS while supported its
72 presence in VS *(Ejdrup et al., 2023; Jorgensen et al., 2023)*. Despite these reported
73 differences in striatal DA dynamics, electrophysiological recordings suggest that DA neurons
74 from the primary innervators of DS, substantia nigra par compacta (SNc) and VS, ventral
75 tegmental area (VTA), have remarkably similar firing patterns at rest *(Dodson et al, 2016)*.
76 We therefore set out to better understand the fundamental principles governing
77 extracellular DA dynamics by constructing a new computational model of the striatal DA
78 system.

79 Extracellular DA dynamics have been modelled before; either one-dimensionally or
80 with a primary focus on single release events or post-synaptic receptor binding *(Beyene et*
81 *al, 2017; Dreyer et al, 2010; Dreyer & Hounsgaard, 2013; Dreyer et al, 2016; Venton et al,*
82 *2003; Wiencke et al, 2020)*. Here, we present a three-dimensional model of tens of
83 thousands of release sites, focused on larger-scale signalling and based on experimentally
84 observed biological parameters. The model faithfully replicates experimentally observed
85 results as well as the difference in DA dynamics between DS and VS. Importantly, it offers
86 compelling evidence that these differences do not primarily reflect different release
87 phenomena but rather arise from differential expression and possibly nanoscale localization
88 of the DA transporter (DAT).

Results

Construction of a model of DA dynamics in the striatum

We constructed a novel model of DA release using experimentally determined parameters from DS, including release, uptake, and cytoarchitecture *(Doucet et al, 1986; Dreyer et al., 2010; Dreyer & Hounsgaard, 2013; Liu et al., 2021; Olson et al, 1972; Sulzer et al., 2016)*. DA release sites on axons projecting from the midbrain were randomly simulated as uniformly distributed discrete points in a three-dimensional space (Figure 1A). The release events themselves were simulated as point source events *(Cragg & Rice, 2004)* driven by action potentials (AP). We then modelled DA release for each voxel in the simulation containing a release site as function of three key parameters; firing rate, release probability and quantal size:

(1)

$$\mathrm{release}_{n,t} = \mathrm{Poisson}(f_{rate}\ dt)_n\ P(R_{\%})_t\ Q\ dt$$

where $\mathrm{Poisson}(f_{rate}\ dt)_n$ is a Poisson distribution of action potentials (AP) for the given neuron (n) with the firing rate f_{rate}(*23*), $P(R_{\%})_t$ is the probability of release at the individual terminal (t) for each AP, while Q is the number of DA molecules released per event (dopaminergic quantal size) and dt the time step. Changing f_{rate} can be used to model both pacemaker firing, typically reported at 2-10 Hz, and burst firing, which can exceed 20 Hz *(Sulzer et al., 2016)*.

DA reuptake in the striatum is almost exclusively mediated by the DA transporter (DAT) *(Jones et al, 1998)*, which is widely distributed along DA axons and varicosities *(Block et al, 2015; Eriksen et al, 2010; Eriksen et al, 2009)*. As reuptake follows concentration-dependent Michaelis-Menten kinetics *(Nicholson, 1995)*, we simulated uptake as follows:

(2)

$$\text{uptake} = \frac{V_{max}\ [DA]}{K_m\ +\ [DA]}\ dt$$

where $[DA]$ is the concentration of DA for each voxel in the model, V_{max} is the maximal uptake capacity in the region and K_m is the concentration of DA at which half of V_{max} is reached.

The spatial distribution of released DA is a complex interplay between release, uptake and diffusion. Diffusion in an open 3D space can be simulated for each voxel with a Laplacian operator:

(3)

$$\text{diffusion} = \frac{\partial DA_{x,y,z,t}}{\partial t} = D_a\ dt\left(\frac{\partial^2 DA_{x,y,z,t}}{\partial x^2} + \frac{\partial^2 DA_{x,y,z,t}}{\partial y^2} + \frac{\partial^2 DA_{x,y,z,t}}{\partial z^2}\right)$$

where D_a is a corrected diffusion coefficient and *dt* is the timestep. As the extracellular space of the striatum is tortuous, we modified the conventional diffusion coefficient D to an apparent diffusion coefficient (D_a) to correct for the tortuosity (λ) of the striatum *(Cragg & Rice, 2004; Nicholson, 1985)*:

(4)

$$D_a = \frac{D}{\lambda^2}$$

Combining equation 1 through 4, we model DA changes in each voxel with a single conceptual equation:

(5)

$$\frac{dDA}{dt} = \text{release} - \text{uptake} + \text{diffusion}$$

We first compared our 3D model of DA dynamics to the analytical solution of a single release event *(Cragg & Rice, 2004; Gonon et al., 2000)*. To do this, we simulated a quantal

event of 3000 DA molecules and calculated DA concentrations across space at three separate time points (Figure 1B, C). The analytic solution and our model predicted almost identical results. Slight differences were introduced as the analytical solution assumes linear uptake from DAT while our model incorporate non-linear Michaelis-Menten kinetics. These differences, however, were almost negligible. The main difference between the two models lies in scalability across both space and time. Summarized, the model enables a dynamic incorporation of the surrounding DA concentration, release events and uptake, and can be scaled to cover DA dynamics of a large 3D space, whose size and granularity is only limited by computing power (see Code Availability Section for the Python code with numerical implementations of the equations listed and scripts to run the simulations and plot the main figures).

We also tested the validity of our model, by examining the response to electrical stimulation. Importantly, our model faithfully mirrored DA release seen with fast-scan cyclic voltammetry (FSCV) recordings upon direct stimulation of striatal slices when we corrected for kinetics of the typical FSCV recording setup (Figure S1b, c and discussion in Supplementary Information) *(Atcherley et al, 2015; Brimblecombe et al, 2019; Stuber et al, 2010; Xie et al, 2020)*.

Simulating large scale DA dynamics of the dorsal striatum

To better understand the extracellular DA dynamics that arise from the balance between dopaminergic pacemaker activity and uptake, we simulated DA dynamics in the DS generated by pacemaker activity (4 Hz) of 150 neurons in the midbrain in a 100x100x100 µm space (Figure 1D, see parameters in Table 1). Our simulations yielded a pattern of partially segregated DA hot spots with large fractions of the simulated space devoid of DA,

158 suggesting that release events in DS only elevate DA in the immediate surroundings with
159 DAT-dependent clearance preventing a larger spread in space (Figure 1D). This was also
160 illustrated by a cross-section in time (Figure 1E). In line with our recent in vivo microdialysis
161 experiments, the average DA concentration in the simulations during pacemaker activity
162 was approximately 10 nM *(Ejdrup et al., 2023)*. Further, when we calculated the average
163 concentration of a larger area across time, which fibre photometry conceivably does, the
164 results resembled a tonic DA concentration (Figure S1A). However, our model predicted a
165 spatial distribution that is highly heterogenous and devoid of pervasive resting or tonic DA
166 levels (Figure 1D-F).

167 To ensure our simulations were performed within a sufficiently large space to yield
168 consistent results, we tested different sizes of the simulated area and found a diameter of
169 50 μm to faithfully mimic the results of larger simulations (Figure S2A, B). Additionally, we
170 tested our simulations at different granularity (0.1, 0.5, 1 and 2 μm). The finer the spatial
171 grain, the higher detail close to a release event; however, at a spatial granularity of 1 μm,
172 [DA] deviated by <2% across most percentiles and only by >1 nM above the 99.5th percentile
173 (Figure S2C-F), leading us to use this voxel size for our simulations.

174

175 ## Burst firing and receptor occupancy

176 DA cell bodies are known to fire short bursts of APs, which is a phenomenon strongly linked
177 to reward-prediction error and learning *(Schultz, 2007)*. To gain insights into accompanying
178 extracellular DA dynamics, we simulated three different firing scenarios for a group of
179 terminals within a 10x10x10 μm field encompassing roughly 40 release sites from the
180 randomly simulated 150 neurons: 3 pulses at 10 Hz, 6 pulses at 20 Hz and 12 pulses at 40 Hz
181 (Figure 1G – burst properties matched to be the same duration). Unsurprisingly, peak DA

concentration was reached at the end of the bursts (Figure 1G). The 3 APs/10 Hz bursting scenario generated no significant spill-over of DA outside the region of activity, whereas the 6 APs/20 Hz and 12 APs/40 Hz bursting scenarios markedly overwhelmed uptake (Figure 1G). The relationship between firing rate and the sphere of influence by DA became further evident when plotting maximal concentration of the surrounding space (Figure 1H) and the volume of space with a DA concentration above 100 nM (Figure S1D). We found that the 3 APs/10 Hz stimulation produced DA responses that largely resembled that of a single pulse. In both cases, DA was mostly cleared after 100 ms and the volume exposed to greater than 100 nM was similar (Figure 1G and Figure S1D). In contrast, the high bursting activities caused a frequency-dependent spill-over, where the areas exposed to a DA concentration above 100 nM were 10 and 30 times larger than the terminal origin for 6 APs/20 Hz and 12 APs/40 Hz, respectively. Even after 100 ms, a considerable amount of DA remained in the 12 APs/40 Hz scenario (Figure 1G).

To understand how these DA dynamics could affect the postsynaptic response, we modelled receptor binding. D1 receptors (-Rs) were assumed to have a half maximal effective concentration (EC_{50}) of 1000 nM and we extrapolated the reverse rate constant (K_{off}) to 19.5 s^{-1} based on a linear fit of the recently characterized DA receptor-based sensors (Figure S1E) *(Labouesse & Patriarchi, 2021)*. We set the EC_{50} of D2Rs to 7 nM and K_{off} to 0.2 s^{-1} based on the DA sensor kinetic fit (Figure S1E), which matches a recent binding study *(Agren et al, 2021)*. To determine how these receptors would respond to our predicted DA dynamics, we simulated pacemaker activity at 4 Hz with an added burst of 6 APs/20 Hz. Figure 1I shows a representative trace of DA concentration and occupancy of the D1R and D2R within 1 µm of a release site. During pacemaker activity, D1R showed an occupancy close to 0, whereas D2R occupancy was approximately 0.65 (Figure 1I). Both D1Rs and D2Rs

206 occupancies were largely invariant to individual release events caused by pacemaker
207 activity. However, upon coordinated burst firing, the occupancy rapidly increased (Figure
208 1I). D1R receptor occupancy closely tracked extracellular DA with a delay of only ~50 ms
209 (Figure S1F). In contrast, it took at least 5 seconds before the burst-induced increase in D2R
210 occupancy had declined to baseline levels (Figure 1I), and, perhaps more surprisingly, the
211 D2R occupancy only fell from 0.55 to 0.45 when simulating a full second pause in firing due
212 to the slow off kinetics (Figure 1J).

213 These simulations suggest that the dopaminergic architecture of the DS limits DA
214 overflow during physiologically relevant bursting activity. Further, DA receptors had a
215 temporally mostly uniform response to DA release caused by pacemaker activity with D1R
216 occupancy responding rapidly to both onset and offset extracellular DA concentrations
217 following bursts, while D2R showed seconds-long delays in offset.

218

219 Ventral striatum maintains pervasive DA tone

220 Mounting evidence points to considerable differences in DA dynamics across striatal
221 subregions *(Jorgensen et al., 2023; Mohebi et al., 2024)*, which might reflect differences in
222 the cytoarchitectural and/or molecular dopaminergic make up. In line with this, most
223 studies report lower dopaminergic density in the VS than in DS regardless of methodological
224 modality with a median value of ~90% in VS relative to DS (Table S1). Further, DAT-mediated
225 uptake capacity is reported to be lower in VS with a median capacity at ~30% of DS (Table
226 S2). Consistently, we observed a clear dorsoventral gradient for DAT expression when
227 analysing immunostainings in striatal mouse brain slices from a previous publication
228 *(Sorensen et al, 2021)*(Figure S3A, B). By contrast, the VMAT2 staining only decreased
229 slightly from VS to DS (Figure S3A-C).

230 We simulated DA release during pacemaker activity in both DS and VS. DS values
231 were set as previously described (25 μm^3 per terminal, uptake capacity of 6.0 $\mu M\ s^{-1}$), but
232 for VS we reduced the terminal density to 90% (27.8 μm^3 per terminal) and DAT uptake
233 capacity to 33% (2.0 $\mu M\ s^{-1}$) (Tables S1 and S2). The remaining parameters were kept
234 identical. With these two differences, our simulations revealed markedly different
235 spatiotemporal DA distributions during pacemaker activity. While DS formed segregated
236 domains with low DA concentrations in the inter-domain space (Figure 2A), DA diffused
237 further throughout the simulated space in VS, before being cleared by DAT. This gave rise to
238 what may be considered a tonic DA level with hotspots of higher DA concentrations (Figure
239 2A, B).
240 We compared our model of the two regions with existing experimental data. In an
241 earlier study by May and Wightman, 120 stimulus pulses were delivered in the medial
242 forebrain bundle (MFB) at either 10, 30 or 60 Hz and DA responses were recorded by FSCV
243 in both caudate-putamen (CPu) and nucleus accumbens (NAc) *(May & Wightman, 1989)*. To
244 mirror this, we simulated 120 action potentials at similar frequencies (10, 30, and 60 Hz) at
245 6% release probability and ran the result through convolution, as in Figure S1B and C, to
246 generate an FSCV read-out (Figure 2E). Since May and Wightman reported no significant
247 difference in DA released per electrically delivered pulse ($[DA]_p$) between VS and DS, we
248 applied equal quantal size and $R_{\%}$ for DS and VS in our simulations, while uptake capacity in
249 VS was kept to a third of DS and terminal density was set to 90% as specified above.
250 Importantly, our simulated FSCV data closely resembled the earlier findings, with VS
251 reaching considerably higher DA levels for all three stimulation frequencies (Figure 2E). This
252 regional difference presumably arises from differences in DAT capacity between DS and VS,

253 as the lower terminal density in VS would have the opposite effect (see below) and the
254 remaining parameters were held identical.
255 To compare with our results for DS, we tested how VS responded during simulated
256 burst activity. Using firing patterns identical to the DS simulations (Figure 1G), we found a
257 larger spill-over of DA into the surrounding areas in VS (Figure 2F and Figure S3D, E).
258 Significant amounts of extracellular DA also remained 100 ms after the physiologically
259 relevant 6APs/20Hz firing stimulus. At the receptor level, D1R occupancy in VS showed a
260 similar response to that in DS during the burst (Figure 1I and 2G). By contrast, D2R
261 occupancy during pacemaker activity was higher in VS than DS (~0.8 versus ~0.65 in DS), in
262 accordance with the higher prevailing basal DA concentration. Additionally, the larger DA
263 overflow in VS after a burst caused a higher relative increase in receptor occupancy further
264 away from the area actively bursting than compared to DS (Figure 2H). A pause in firing had
265 the same effect on D2R as in DS (Figure S3F).
266

267 ## Testing sensitivity of model parameters

268 To test the robustness of the results, we performed simulations across wide ranges of the
269 variable key parameters on which the model is based. First, we varied the number of
270 varicosities actively releasing DA by setting the varicosity density to one site per 9 μm^3
271 *(Doucet et al., 1986)* and simulating 4 Hz pacemaker activity with the release fraction
272 ranging from 5% to 100% (reported values range from 20% to virtually all) *(Ducrot et al,*
273 *2021; Liu et al., 2021; Liu et al, 2018; Pereira et al, 2016)* (Figure 3A). As the fraction of
274 active sites increased, DA concentrations increased at both the median level (50th
275 percentile), which we consider a measure of tonic or baseline DA levels, and at peak levels
276 (99.5^{th} percentile) in both DS and VS (Figure 3B, see Figure S4A for schematic of tonic and

277 peak DA). We then used the 99.5th/50th percentile ratio as a measure of the focality of the
278 DA distribution (i.e. hotspot DA relative to baseline DA). Quantifying this across the
279 percentage of active terminals showed that the focality of the DA distribution dropped as
280 the active fraction increased in both regions (Figure 3C). However, the percentage of active
281 sites in VS needed to drop to 5% to reach a relative distribution resembling the DS at a full
282 100% active sites, underscoring a marked difference in the spatial confinement of DA signals
283 in VS and DS.

284 The predicted total DA content of a vesicle and the fraction of content released per
285 fusion event is reported to range from 1,000 to 30,000 molecules *(Garris et al, 1994; Pothos*
286 *et al, 1998; Staal et al, 2004; Sulzer & Pothos, 2000)* (Figure 3D). As expected, tonic and peak
287 concentrations increased in both DS and VS as quantal size was increased (Figure 3E). Also
288 as expected, the focality of the DA distributions dropped for both regions as quantal size
289 increased (Figure 3F). The relative difference in tonic DA, however, remained persistently
290 higher in VS and even increased as quantal size increased, indicating a tendency for VS to
291 maintain basal levels of DA regardless of release content (Figure 3G). The higher end of
292 quantal sizes, however, resulted in median concentrations far beyond what is typically
293 reported (Figure 3E) *(Sulzer et al., 2016)*. We observed largely similar pattern when changing
294 either release probability or firing rate (Figure S4B-G).

295 DAT activity is governed by two parameters: K_m and V_{max} *(Kristensen et al, 2011)*. To
296 mimic competitive inhibition of DAT by e.g., cocaine, we ran a simulation across various K_m
297 values (Figure 3H) showing that increasing K_m caused a linear increase in DA levels,
298 consistent with DAT uptake rate responding almost linearly to increases in [DA] below K_m
299 (Figure 3I). Of note, most microdialysis studies have reported that cocaine increases [DA] to
300 the same degree in both DS and VS; however, these quantifications are usually derived as a

301 ratio of the absolute baseline level *(Carboni et al, 2001; Maisonneuve & Glick, 1992)*. If we
302 divide our simulations of increasing K_m with the basal levels estimated in Figure 3A-C a
303 similar response for DS and VS is found (Figure 5A). Further, we observe a convergence on a
304 two-fold difference in the absolute values at both tonic and peak levels, which matches
305 reports from earlier FSCV studies (Figure S5B) *(Wu et al, 2001)*. This regionally differential
306 response to cocaine matches our observations in a previous biosensor-based study
307 *(Jorgensen et al., 2023)*.

308 Finally, we changed V_{max} by ± 50% in both regions and observed a smaller change in
309 for tonic level in DS (11 nM) than in VS (38 nM) (Figure 3K). This suggests modulation of V_{max}
310 has higher impact in VS than DS. Further, the cusp-like behaviour of V_{max} in VS was
311 independent of both Q and $R_{\%}$ within values typically reported in the literature (Figure S5C,
312 D). In contrast to the changes in tonic levels, the relative effect V_{max} had on peak levels was
313 much more modest (Figure 3L).

314 Changes to uptake rate may be mediated by DAT internalization pathways but to our
315 knowledge there is not in vivo evidence of differential release-uptake balances between
316 animals that could lead to varying tonic DA levels across animals. We therefore reanalysed
317 data from our previously published comparison of fibre photometry and microdialysis and
318 found evidence of natural variations in the release-uptake balance of the mice (Figure 5F,
319 G), which may underlie different tonic levels of DA in the striatum between animals.

320

321 ## Simulations of DAT nanoclustering

322 Our simulations highlight DAT V_{max} as an effective regulator of extracellular DA levels in VS
323 (Figure 3K). Internalization of DAT can serve as a mechanism for this control but is a
324 relatively slow process operating on the order of minutes *(Kristensen et al., 2011)*.

325 Interestingly, our recent studies have provided evidence that DAT move laterally in the
326 plasma membrane and transition from a clustered to an unclustered nanoscale distribution
327 in response to excitatory drive and other inputs *(Lycas et al, 2022; Rahbek-Clemmensen et*
328 *al, 2017)*. This led us to hypothesize that DAT nanoclustering serve as a mechanism for
329 regulating DAT activity on a faster time scale. We speculated that dense nanoclusters of DAT
330 would produce domains of low [DA] due to uptake overpowering diffusion (Figure 4A). As
331 uptake rate is concentration dependent, this would reduce uptake efficiency (Figure 4B). To
332 address this hypothesis, we simulated a single ellipsoid varicosity of 1.5 μm in length and
333 800 nm thick with surrounding extracellular space *(Ducrot et al., 2021)*. The surface was
334 unfolded to a square of equal area (Figure 4D), and as 9-16.4% of terminals in the striatum
335 are estimated to be dopaminergic *(Hokfelt, 1968; Tennyson et al, 1974)*, we set the volume
336 of the surrounding space to seven times the varicosity volume. On the surface of the
337 varicosity, we randomly distributed eight DAT nanoclusters (Figure 4C) and ran simulations
338 of how DAT clustering density influenced the DA clearance from the surrounding space. The
339 observed DA concentration in the space surrounding the varicosity shown in Figure 4C is
340 illustrated by the cross-section shown in Figure 4D. Mean DA uptake capacity of the entire
341 space was kept constant at 4 $\mu M\ s^{-1}$ (between the values observed for DS and VS)
342 throughout the simulations, representing a constant amount of DAT molecules on the
343 surface of the varicosity. We only changed the fraction of the surface of the varicosity that
344 was uptake competent by altering the cluster size from small clusters of high density to
345 large clusters of lower density. We ran simulations of eight clusters at 20, 40, 80 or 160 nm
346 in diameter to mirror experimentally observed cluster sizes on DA varicosities, as well as a
347 scenario with DAT fully dispersed (Figure 4E) *(Lycas et al., 2022; Rahbek-Clemmensen et al.,*
348 *2017)*. We then set the extracellular space to a [DA] of 100 nM and simulated uptake for the

349 four cluster sizes and an unclustered distribution of DAT. As shown in Figure 4F, the
350 distribution of DAT into clusters of increasing density resulted in progressively slower DA
351 clearance. Thus, the unclustered scenario reduced [DA] to 10 nM in just above 200 ms,
352 whereas the 20 nm clusters took ~400 ms. As cluster size increased and DAT density
353 decreased, clearance time approached that of the fully unclustered scenario (Figure 4G).
354 The resulting hyper-local low-[DA] environment that came from dense DAT clusters was
355 apparent when we plotted the [DA] at the centre of a cluster compared to the mean [DA] of
356 the extracellular space (Figure 4H). For the 20 nm cluster-scenario, the clearance was almost
357 entirely limited by how quickly DA diffused to the nanocluster, as the local [DA] dropped to
358 near zero. We originally hypothesized the effect would mainly be due to a depression in
359 [DA] at the cluster centre, but a concentration profile of the 80 nm cluster-scenario revealed
360 the entirety of the cluster was enveloped in a low-[DA] environment (Figure 4I).
361 Summarized, the data supports that dense DAT nanoclusters produce domains of
362 low [DA] as uptake outcompetes diffusion. With transporter uptake being concentration
363 dependent, uptake efficiency is reduced. The simulations therefore posit DAT
364 nanoclustering as an efficient way to regulate the extracellular levels of tonic DA,
365 particularly in VS.
366

367 ## DAT clusters more in the ventral striatum

368 As our simulations suggest that nanodomain clustering is a way of regulating uptake, and
369 this may be particularly efficient at controlling extracellular DA in VS, we hypothesized
370 nanoscale clustering would be more prominent in VS. To investigate this, we reanalysed
371 data from a previous publication*(Sorensen et al., 2021)*, where we acquired super-resolution
372 images of coronally sliced striatal sections from mice stained for DAT. For the present study,

373 images were split in DS and VS based on where in the slices they were taken (Figure 4J). DA
374 terminals were identified by vesicular monoamine transporter 2 (VMAT2) expression, and
375 qualitatively DAT appeared more clustered in VS than DS (Figure 4K). To quantify this, we
376 applied the clustering algorithm Density-Based Spatial Clustering of Applications with Noise
377 (DBSCAN) (Figure 4L). This confirmed a regional difference with more DAT localized to mean
378 cluster size of 80 nm in VS compared to DS (Figure 4M), and we observed a similar regional
379 difference across the range of sizes typically reported (Figure 4N) *(Lycas et al., 2022;*
380 *Rahbek-Clemmensen et al., 2017)* supporting the conclusion that DAT nanoclustering is
381 more prevalent in VS than DS.

382 ## Discussion

383 We developed a three-dimensional, finite-difference computational model to investigate
384 spatiotemporal DA dynamics of striatal subregions in detail. Leveraging prior experimental
385 information on regional differences in dopaminergic innervation density and DAT uptake
386 capacity, our model predicts important differences in dopaminergic dynamics between DS
387 and VS. Strikingly, our simulations suggest that large areas of the DS are effectively devoid
388 of a basal level of DA at pacemaker activity, whereas VS maintain a more homogenous
389 tonic-like basal DA concentration with only small changes in uptake activity powerfully
390 regulating the extracellular DA tone. Furthermore, we modelled receptor binding kinetics
391 and found that D1R binding faithfully followed recently described rapid DA dynamics of the
392 striatum *(Ejdrup et al., 2023; Jorgensen et al., 2023; Markowitz et al, 2023)*, while D2R, with
393 an off-rate of ~5 seconds, appeared better suited for detecting background tone, ramps and
394 integrating prolonged activity *(Howe et al, 2013; Jorgensen et al., 2023)*. Collectively, these
395 observations have important implications for our understanding of striatal function in
396 behaviour, including decoding of inputs from the prefrontal cortex (PFC) and limbic system
397 as well as the influential phasic-tonic model of dopaminergic signalling *(Grace et al, 2007;*
398 *Niv et al., 2007; Schultz, 2007)*

399 It has been assumed for long that there are tonic levels of DA in the striatum *(Niv et*
400 *al., 2007; Schultz, 2007; Sulzer et al., 2016)*, although the phenomenon has no clear
401 definition (*1*). Our simulation of DA dynamics in DS during pacemaker-activity showed no
402 evidence for a homogenous extracellular distribution. Rather, elevated [DA] was transiently
403 present around release sites during pacemaker activity with the remaining space mostly
404 depleted of DA. The absence of a general tonic DA level in DS predicted by our model

405 directly supports the notion that DA release sites in DS establish distinct and only partially
406 overlapping DA domains rather than diffuse, tonic DA levels (see Liu et al., 2021 *(Liu et al.,*
407 *2021)*. This conclusion aligns with recent data where we found that DA concentrations
408 measured by microdialysis correlates with the average of rapid activity recorded with fibre
409 photometry rather than a baseline DA tone *(Ejdrup et al., 2023)*.

410 In contrast to the DS, our model predicted VS to hold a considerable basal level of DA
411 even in spaces without an immediately adjacent release site. This is conceivably what most
412 refer to as tonic DA. In this study, we quantified tonic DA as the median concentration of the
413 entire space (50th percentile), which appeared significantly higher in VS than DS because of
414 the lower VS uptake capacity. Importantly, this matches the results of our direct in vivo
415 comparison of DS and VS in freely moving mice *(Jorgensen et al., 2023)*. To challenge our
416 model, we performed our simulations across a wide range of parameters. Only changes to
417 V_{max} for uptake generated differential responses in the two regions. With release and
418 uptake parameters at values from the literature, VS was at a critical point where minor
419 changes to uptake significantly impacted the tonic levels without any major effect on peak
420 concentrations.

421 Contrary to our observations, some previous microdialysis experiments have
422 suggested higher basal DA levels in the DS compared to VS (Kuczenski & Segal, 1992; Shen et
423 al., 2004 have reported 2-4 times higher [DA] in DS compared to VS *(Kuczenski & Segal,*
424 *1992; Shen et al, 2004)*.However, there are disparate observations in the literature (e.g.
425 Carboni et al., 2001 reported 20% higher [DA] in VS *(Carboni et al., 2001)*. Moreover, it is
426 important to note that regional comparisons in microdialysis might be confounded by the
427 considerably higher uptake rate in DS. This will increase the extraction fraction and possibly

428 lead to a significant overestimation of the extracellular concentration as compared to a
429 region with lower uptake rate, such as the VS *(Chefer et al, 2009)*.
430 Our three-dimensional simulations highlight DAT-mediated reuptake as a key
431 mechanism governing striatal DA dynamics and as a key mediator of regional-specific DA
432 dynamics. A physiologically relevant way to regulate uptake capacity is moving DAT to-and-
433 from the plasma membrane. Indeed, DAT is subject to such regulation and some of these
434 mechanisms may even be exclusive to the ventral region, including protein kinase C-induced
435 DAT internalization and Vav2 regulation of DAT surface expression *(Fagan et al, 2020; Zhu et*
436 *al, 2015)*. Chemogenetic G_q-coupled DREADD activation of DA neurons also result in
437 differential DAT trafficking in the two regions *(Fagan et al., 2020; Kearney et al., 2023)*. The
438 findings position DAT regulation as an excellent candidate for changing tonic DA levels in VS,
439 which has been proposed to selectively attenuate afferent drive from the PFC through D2R
440 activation *(Grace et al., 2007)*. Recent studies of D2R expressing spiny projection neurons
441 (SPNs) in the VS also suggest that the receptor is not fully saturated under basal firing *(Lee*
442 *et al, 2020)*, matching both our simulations of receptor binding and the notion that tonic DA
443 can be manipulated to alter D2R activation.
444 If changing uptake capacity is to have a behavioural relevance on a fast timescale, a
445 mechanism to regulate DAT function faster than internalization must exist. Importantly, the
446 transporter does not only move to-and-from the surface, but also laterally in the plasma
447 membrane. We have reported that DAT forms nanoclusters in the plasma membrane that
448 dynamically reshape based on excitatory and inhibitory input *(Lycas et al., 2022; Rahbek-*
449 *Clemmensen et al., 2017)*. Moreover, we have previously shown that cocaine, which both
450 competitively inhibits DAT and reorganizes the transporter nanodomains *(Lycas et al.,*
451 *2022)*, changes the DA signal of the DS to dynamics akin to the VS *(Jorgensen et al., 2023)*.

452 Importantly, our simulations showed that nanoclustering may be an effective way to
453 sequester DAT in a dense domain where uptake overpowers diffusion and as a result brings
454 down effective uptake speed through microdomain DA depletion. This is in line with
455 evidence that these DAT nanoclusters are enriched in phosphatidylinositol-4,5-bisphosphate
456 (PIP2), and that metabolism of PIP2 decreases uptake rate of DAT *(Lycas et al., 2022)*;
457 Carvelli, 2002 #2339}. We also found that the nanoclustering phenomenon was considerably
458 more prevalent in VS than in DS. Taken together, these data point to DAT nanoclustering as
459 a way to shape tonic levels of DA in the striatum – particularly in the VS.

460 Our incorporation of receptor binding was inspired by previous data *(Dreyer et al.,*
461 *2010; Dreyer & Hounsgaard, 2013; Hunger et al, 2020)*. Dreyer & colleagues assumed
462 instantaneous equilibrium between extracellular DA and receptor occupation while Hunger
463 & colleagues based their kinetics on early pharmacological studies *(Burt et al, 1976; Maeno,*
464 *1982; Nishikori et al, 1980; Sano et al, 1979)*. However, we based our receptor kinetics on
465 newer pharmacological experiments in live cells *(Agren et al., 2021)* and properties of the
466 recently developed DA receptor-based biosensors *(Labouesse & Patriarchi, 2021)*. Indeed,
467 these sensors are mutated receptors but only on the intracellular domains with no changes
468 of the binding site *(Labouesse & Patriarchi, 2021)*. Overall, they exhibit kinetics that are well
469 aligned with both modelled and experimentally reported extracellular DA dynamics using
470 non-biosensor-based methods *(Atcherley et al., 2015; Gonon et al., 2000; Venton et al,*
471 *2002)*.

472 The presented simulations suggested that receptor binding was largely invariant to
473 single release events during pacemaker activity, while bursts of activity rapidly changed
474 occupancy. Both D1R and D2R immediately responded to burst onset; however, while D1R
475 occupancy rapidly declined to zero within approximately 50 ms, the slow D2R kinetics

476 resulted in an occupancy decline over ~5 seconds, returning to the baseline maintained by
477 tonic firing. This means that D1R is better suited to discriminate inputs in rapid succession
478 and allow for postsynaptic decoding of the fast-paced in vivo dynamics described in
479 particularly for DS *(Ejdrup et al., 2023; Jorgensen et al., 2023; Markowitz et al., 2023)*. By
480 contrast, our analysis shows that D2Rs integrate DA signals over several seconds. As D1R
481 occupancy is negligible during pacemaker activity and D2R kinetics are too slow to pick up
482 rapid changes in DA concentration, our simulations moreover suggest pauses in firing of less
483 than 1 second is not an effective way of signalling for the striatal dopaminergic system.
484 In conclusion, we have developed a three-dimensional model for DA release
485 dynamics and receptor binding that integrates a wealth of experimentally determined
486 parameters and generates responses to electrical and pharmacological input that fits
487 robustly with literature observations. The model offers an important theoretical framework
488 and a predictive tool that can serve as the basis for future experimental endeavours and
489 help guide the interpretation of new as well as older empirical findings on DA signalling
490 dynamics under both physiological conditions and in disease.

491 # Methods

492 ## Three-dimensional finite difference model

493 DA release sites in the striatum were simulated at a density of one site per 25 μm^3 in DS and
494 one site per 27.8 μm^3 in VS (except for Figure 4b and c). As a single medium spiny neuron in
495 the striatum is estimated to be influenced by axons from 95 to 194 dopaminergic neurons
496 *(Matsuda et al, 2009)*, we simulated DA release sites as originating from 150 separate cell
497 bodies. These were set to fire independently from each other at 4 Hz generated by a Poisson
498 distribution. We set the release probability in response to an action potential at the
499 individual terminal levels to 6% *(Dreyer et al., 2010)*, and if a release occurred the DA
500 concentration of the voxel was elevated by the equivalent of 3000 DA molecules as per
501 Equation 1. The volume of each voxel was corrected for an extracellular volume fraction of
502 0.21 *(Rice & Nicholson, 1991)*.

503 We did not incorporate paired-pulse depression in our model as most in vivo FSCV
504 studies have not reported this phenomenon *(Chergui et al, 1994; Garris & Wightman, 1994;*
505 *Hamid et al, 2016; May & Wightman, 1989)*. In addition, we could explain the gradual blunt
506 of the response during prolonged stimulation (Figure 2E) as the result of an equilibrium
507 between release and uptake rather than a depression in release. Newer in vivo biosensor-
508 based studies observe the same "blunting" phenomenon during stimulation trains *(Mohebi*
509 *et al, 2023)*. A low initial release probability that scales well with frequency has also been
510 reported for VMAT2-positive release sites in dopaminergic cultures where the axons are not
511 severed from their cell bodies as in acute striatal slices *(Silm et al, 2019)*. Note that we did
512 not explicitly model autoreceptor inhibition at pacemaker activity. However, this value
513 should be implicitly reflected in the in vivo estimates we base our model on.

514 When simulating bursts or trains of stimulations, action potentials were added as
515 described for each simulation, but release probability was kept the same unless otherwise
516 noted. Uptake was evenly distributed throughout the simulation space with a V_{max} at 6 µm s^{-1}
517 for DS and 2 µm s^{-1} for VS (see Table S2) and a K_m at 210 nM *(Hovde et al, 2019)* and
518 calculated for each voxel as per Equation 2. For each time step, *dt*, diffusion calculated with
519 a finite difference implementation of the Laplacian operator described in Equation 3 using a
520 diffusion coefficient corrected for tortuosity at 321.7 μm^2 s^{-1}. Periodic boundaries were used
521 to avoid edge issues with a simulation size of 50x50x50 µm unless otherwise noted. The
522 Python-based implementation of the model can be found as described in the Code and Data
523 Availability section.
524

525 ## Immunohistochemistry analysis

526 Analysed widefield images were obtained from *(Sorensen et al., 2021)*. The mouse striatum
527 slices were stained for either DAT or VMAT2 (see Sørensen et al., 2021 for slicing, fixation,
528 staining and imaging protocol *(Sorensen et al., 2021)*. Fluorescence intensities were
529 extracted in a single dorsoventral line parallel to the midline through the horizontally centre
530 of the anterior commissure using ImageJ v1.53q. for each slice. Data was vertically centred
531 around the anterior commissure. No background subtraction was performed.
532

533 ## FSCV modelling

534 FSCV recordings were modelled by convoluting a simulated DA response to a pseudo FSCV
535 trace. The impulse function used was as described in *(Venton et al., 2002)*. In brief, the
536 impulse function was defined as $\mathrm{IF_{FSCV}} = e^{-(t+1)(k_{-1}*t_s+k_{-2}*t_o)}$, where t is time, t_s is scan

537 time, t_o is oxidization time, and k_{-1} and k_{-2} desorption constants. t_s was set to 100 ms as
538 reported in *(May & Wightman, 1989)* and t_o to 4 ms, which is half of the typically reported
539 symmetrical waveform length. The desorption constants (k_{-1} = 1.2 s^{-1} and k_{-2} = 12 s^{-1}) were
540 taken directly from *(Venton et al., 2002)*.
541

542 ## Nanocluster uptake modelling

543 Nanoclustering of DAT was simulated in Python. An ellipsoid-shaped varicosity of 1.5 μm in
544 length and 800 nm in width was modelled as a flat, square surface with a width of 1.8 μm to
545 match the total surface area *(Lycas et al., 2022; Rahbek-Clemmensen et al., 2017)*. As 9-
546 16.4% of terminals in the striatum are estimated to be dopaminergic*(Hokfelt, 1968;*
547 *Tennyson et al., 1974)*, we set the height of the simulation space to 3.52 μm to generate an
548 extracellular volume seven times the size of the varicosity. Axons and cell bodies are likely a
549 non-negligible part of the striatal volume but omitted in this analysis due to a lack of
550 information in the literature (however, decreasing the share of striatal space taken up by DA
551 varicosities works in the direction of our hypothesis). Spatial granularity was set to 20 nm,
552 and we randomly placed eight non-overlapping locations for clusters on the simulated
553 varicosity. Uptake capacity per voxel for each clustering scenario was set so the mean
554 uptake of the entire space was 4 μm s^{-1}, which resulted in clusters with increased DAT
555 density with decreasing cluster size. We set the initial DA concentration of the entire space
556 to 100 nM and ran the simulation with a time step of 1.875e^{-7} s to avoid numerical
557 instability. Diffusion corrected for tortuosity was set to 321.7 μm^2 s^{-1} and calculated with a
558 Laplacian operation as described in Equation 3. Periodic boundaries were used to account
559 for the varicosity being circular and avoid issues at the edge of the simulation space. The full

560 implementation in Python can be found as described in the Code and Data Availability
561 section.
562

563 ## Super-resolution clustering analysis

564 Super-resolved fluorescence microscopy dual color images from *(Sorensen et al., 2021)* of
565 striatal brain slices from mice were analyzed based on their position in the dorsal or ventral
566 regions (Figure 4J). Localizations were fitted using DAOSTORM *(Babcock et al, 2012)* on the
567 originally acquired direct stochastic optical reconstruction microscopy (dSTORM) videos
568 with the following settings: background sigma of 8, maximum likelihood estimation as the
569 fitting error model, 20 peak identification iterations, an initial sigma estimate of 1.5 and a
570 threshold adjusted to each imaging session. Each image was analysed for percentage of
571 localizations within a cluster using density-based spatial clustering of applications with noise
572 (DBSCAN) *(Ester et al, 1996)* using the Python package Scikit-learn 0.22 *(Pedregosa et al,*
573 *2021)*. To uncover broader trends, we scanned across a range of parameters: radius was run
574 from 10 nm to 200 nm and number of localizations from 10 to 200. For Figure 4M a
575 diameter of 80 nm was chosen to match the size reported in *(Rahbek-Clemmensen et al.,*
576 *2017)*.
577

578 ## Statistical Analysis

579 The statistical analyses performed can be found in the legends of each figure. Statistical
580 analyses were performed using open-source python packages SciPy v1.5.2 and NumPy
581 v1.18.1. Boxplots show the 25th and 75th percentile range and whiskers indicate up to 1.5
582 times the interquartile range. The remaining data points are plotted as individual outliers.
583

Acknowledgements

We thank Dr. Kenneth L. Madsen, University of Copenhagen for general input on our modelling and Dr. Nicolas Tritsch, New York University Grossman School of Medicine, for a fruitful discussion on the postsynaptic receptor properties and occupation.

Additional Information

Competing Interest

Authors declare that they have no competing interests

Funding

The work was supported by the Lundbeck Foundation grants R266-2017-4331 (UG), R276-2018-792 (UG), R359-2020-2301 (UG), R181-2014-3090 (FH) and R303-2018-3540 (FH).

Author Contributions

ALE, FH and UG conceptualized the study. ALE built the model with help from JKD. ALE ran the simulations. MDL and SHJ provided technical input on experimental data. ALE drafted the manuscript. ALE, FH and UG wrote the final version of the manuscript with comments and suggestions from JKD, TWR and JWD. All authors critically evaluated the manuscript. FH and UG supervised the project.

Additional files

Supplementary file

Supplementary Text

Figures. S1 to S5

Tables S1 and S2

Data Availability

Numerical implementation and code to run the simulations are available at: https://github.com/GetherLab/striatal-dopamine-modelling. All experimental data are from Ejdrup & Wellbourne-Wood et al. *(Ejdrup et al., 2023)*, 2023 or Sørensen et al., 2021 *(Sorensen et al., 2021)*. Corresponding authors on these papers should be consulted for data availability.

618 ## References

619 Agnati LF, Bjelke B, Fuxe K. 1995. Volume versus wiring transmission in the brain: a new
620 theoretical frame for neuropsychopharmacology. *Med Res Rev* **15**: 33-45.
621 10.1002/med.2610150104

622 Agren R, Stepniewski TM, Zeberg H, Selent J, Sahlholm K. 2021. Dopamine D(2) Receptor
623 Agonist Binding Kinetics-Role of a Conserved Serine Residue. *Int J Mol Sci*
624 **22**10.3390/ijms22084078

625 Atcherley CW, Laude ND, Monroe EB, Wood KM, Hashemi P, Heien ML. 2015. Improved
626 Calibration of Voltammetric Sensors for Studying Pharmacological Effects on Dopamine
627 Transporter Kinetics in Vivo. *ACS Chem Neurosci* **6**: 1509-1516. 10.1021/cn500020s

628 Babcock H, Sigal YM, Zhuang X. 2012. A high-density 3D localization algorithm for stochastic
629 optical reconstruction microscopy. *Opt Nanoscopy* **1**10.1186/2192-2853-1-6

630 Berke JD. 2018. What does dopamine mean? *Nat Neurosci* **21**: 787-793. 10.1038/s41593-018-
631 0152-y

632 Beyene AG, McFarlane IR, Pinals RL, Landry MP. 2017. Stochastic Simulation of Dopamine
633 Neuromodulation for Implementation of Fluorescent Neurochemical Probes in the Striatal
634 Extracellular Space. *ACS Chem Neurosci* **8**: 2275-2289. 10.1021/acschemneuro.7b00193

635 Block ER, Nuttle J, Balcita-Pedicino JJ, Caltagarone J, Watkins SC, Sesack SR, Sorkin A. 2015.
636 Brain Region-Specific Trafficking of the Dopamine Transporter. *J Neurosci* **35**: 12845-12858.
637 10.1523/JNEUROSCI.1391-15.2015

638 Borroto-Escuela DO, Perez De La Mora M, Manger P, Narvaez M, Beggiato S, Crespo-Ramirez
639 M, Navarro G, Wydra K, Diaz-Cabiale Z, Rivera A *et al*. 2018. Brain Dopamine Transmission in
640 Health and Parkinson's Disease: Modulation of Synaptic Transmission and Plasticity Through
641 Volume Transmission and Dopamine Heteroreceptors. *Front Synaptic Neurosci* **10**: 20.
642 10.3389/fnsyn.2018.00020

643 Brimblecombe KR, Vietti-Michelina S, Platt NJ, Kastli R, Hnieno A, Gracie CJ, Cragg SJ. 2019.
644 Calbindin-D28K Limits Dopamine Release in Ventral but Not Dorsal Striatum by Regulating
645 Ca(2+) Availability and Dopamine Transporter Function. *ACS Chem Neurosci* **10**: 3419-3426.
646 10.1021/acschemneuro.9b00325

647 Brown HD, McCutcheon JE, Cone JJ, Ragozzino ME, Roitman MF. 2011. Primary food reward
648 and reward-predictive stimuli evoke different patterns of phasic dopamine signaling
649 throughout the striatum. *Eur J Neurosci* **34**: 1997-2006. 10.1111/j.1460-9568.2011.07914.x

650 Burt DR, Creese I, Snyder SH. 1976. Properties of [3H]haloperidol and [3H]dopamine binding
651 associated with dopamine receptors in calf brain membranes. *Mol Pharmacol* **12**: 800-812.

652 Carboni E, Spielewoy C, Vacca C, Nosten-Bertrand M, Giros B, Di Chiara G. 2001. Cocaine and
653 amphetamine increase extracellular dopamine in the nucleus accumbens of mice lacking the
654 dopamine transporter gene. *J Neurosci* **21**: RC141: 141-144. 20015177 [pii]

655 Cardozo DL, Bean BP. 1995. Voltage-dependent calcium channels in rat midbrain dopamine
656 neurons: modulation by dopamine and GABAB receptors. *J Neurophysiol* **74**: 1137-1148.
657 10.1152/jn.1995.74.3.1137

658 Chefer VI, Thompson AC, Zapata A, Shippenberg TS. 2009. Overview of brain microdialysis.
659 *Curr Protoc Neurosci* **Chapter 7**: Unit7 1. 10.1002/0471142301.ns0701s47

660 Chergui K, Suaud-Chagny MF, Gonon F. 1994. Nonlinear relationship between impulse flow,
661 dopamine release and dopamine elimination in the rat brain in vivo. *Neuroscience* **62**: 641-
662 645. 10.1016/0306-4522(94)90465-0

663 Cragg SJ, Rice ME. 2004. DAncing past the DAT at a DA synapse. *Trends Neurosci* **27**: 270-277.
664 10.1016/j.tins.2004.03.011

665 Dodson PD, Dreyer JK, Jennings KA, Syed EC, Wade-Martins R, Cragg SJ, Bolam JP, Magill PJ.
666 2016. Representation of spontaneous movement by dopaminergic neurons is cell-type
667 selective and disrupted in parkinsonism. *Proc Natl Acad Sci U S A* **113**: E2180-2188.
668 10.1073/pnas.1515941113

669 Doucet G, Descarries L, Garcia S. 1986. Quantification of the dopamine innervation in adult
670 rat neostriatum. *Neuroscience* **19**: 427-445. 10.1016/0306-4522(86)90272-1

671 Dreyer JK, Herrik KF, Berg RW, Hounsgaard JD. 2010. Influence of Phasic and Tonic Dopamine
672 Release on Receptor Activation. *Journal of Neuroscience* **30**: 14273-14283. Doi
673 10.1523/Jneurosci.1894-10.2010

674 Dreyer JK, Hounsgaard J. 2013. Mathematical model of dopamine autoreceptors and uptake
675 inhibitors and their influence on tonic and phasic dopamine signaling. *J Neurophysiol* **109**:
676 171-182. 10.1152/jn.00502.2012

677 Dreyer JK, Vander Weele CM, Lovic V, Aragona BJ. 2016. Functionally Distinct Dopamine
678 Signals in Nucleus Accumbens Core and Shell in the Freely Moving Rat. *J Neurosci* **36**: 98-112.
679 10.1523/JNEUROSCI.2326-15.2016

680 Ducrot C, Bourque MJ, Delmas CVL, Racine AS, Guadarrama Bello D, Delignat-Lavaud B,
681 Domenic Lycas M, Fallon A, Michaud-Tardif C, Burke Nanni S *et al*. 2021. Dopaminergic
682 neurons establish a distinctive axonal arbor with a majority of non-synaptic terminals. *FASEB*
683 *J* **35**: e21791. 10.1096/fj.202100201RR

684 Ejdrup AL, Wellbourne-Wood J, Dreyer JK, Guldhammer N, Lycas MD, Gether U, Hall BJ,
685 Sorensen G. 2023. Within-Mice Comparison of Microdialysis and Fiber Photometry-Recorded
686 Dopamine Biosensor during Amphetamine Response. *ACS Chem Neurosci* **14**: 1622-1630.
687 10.1021/acschemneuro.2c00817

688 Eriksen J, Jorgensen TN, Gether U. 2010. Regulation of dopamine transporter function by
689 protein-protein interactions: new discoveries and methodological challenges. *J Neurochem*
690 **113**: 27-41. 10.1111/j.1471-4159.2010.06599.x

691 Eriksen J, Rasmussen SG, Rasmussen TN, Vaegter CB, Cha JH, Zou MF, Newman AH, Gether U.
692 2009. Visualization of dopamine transporter trafficking in live neurons by use of fluorescent
693 cocaine analogs. *J Neurosci* **29**: 6794-6808. 29/21/6794 [pii]
694 10.1523/JNEUROSCI.4177-08.2009

695 Ester M, Kriegel H-P, Sander J, Xu X (1996) A density-based algorithm for discovering clusters
696 in large spatial databases with noise. In: *Proc 2nd International Conference on Knowledge*
697 *Discovery and Data Mining*, pp. 226–231. AAAI Press:

698 Fagan RR, Kearney PJ, Sweeney CG, Luethi D, Schoot Uiterkamp FE, Schicker K, Alejandro BS,
699 O'Connor LC, Sitte HH, Melikian HE. 2020. Dopamine transporter trafficking and Rit2 GTPase:
700 Mechanism of action and in vivo impact. *J Biol Chem* **295**: 5229-5244.
701 10.1074/jbc.RA120.012628

702 Garris PA, Ciolkowski EL, Pastore P, Wightman RM. 1994. Efflux of dopamine from the synaptic
703 cleft in the nucleus accumbens of the rat brain. *J Neurosci* **14**: 6084-6093.
704 10.1523/JNEUROSCI.14-10-06084.1994

705 Garris PA, Wightman RM. 1994. Different kinetics govern dopaminergic transmission in the
706 amygdala, prefrontal cortex, and striatum: an in vivo voltammetric study. *J Neurosci* **14**: 442-
707 450. 10.1523/JNEUROSCI.14-01-00442.1994

708 Gonon F, Burie JB, Jaber M, Benoit-Marand M, Dumartin B, Bloch B. 2000. Geometry and
709 kinetics of dopaminergic transmission in the rat striatum and in mice lacking the dopamine
710 transporter. *Prog Brain Res* **125**: 291-302. 10.1016/S0079-6123(00)25018-8

711 Grace AA, Floresco SB, Goto Y, Lodge DJ. 2007. Regulation of firing of dopaminergic neurons
712 and control of goal-directed behaviors. *Trends Neurosci* **30**: 220-227.
713 10.1016/j.tins.2007.03.003

714 Hamid AA, Pettibone JR, Mabrouk OS, Hetrick VL, Schmidt R, Vander Weele CM, Kennedy RT,
715 Aragona BJ, Berke JD. 2016. Mesolimbic dopamine signals the value of work. *Nat Neurosci* **19**:
716 117-126. 10.1038/nn.4173

717 Hokfelt T. 1968. In vitro studies on central and peripheral monoamine neurons at the
718 ultrastructural level. *Z Zellforsch Mikrosk Anat* **91**: 1-74. 10.1007/BF00336984

719 Hovde MJ, Larson GH, Vaughan RA, Foster JD. 2019. Model systems for analysis of dopamine
720 transporter function and regulation. *Neurochem Int* **123**: 13-21.
721 10.1016/j.neuint.2018.08.015

722 Howe MW, Tierney PL, Sandberg SG, Phillips PE, Graybiel AM. 2013. Prolonged dopamine
723 signalling in striatum signals proximity and value of distant rewards. *Nature* **500**: 575-579.
724 10.1038/nature12475

725 Hunger L, Kumar A, Schmidt R. 2020. Abundance Compensates Kinetics: Similar Effect of
726 Dopamine Signals on D1 and D2 Receptor Populations. *J Neurosci* **40**: 2868-2881.
727 10.1523/JNEUROSCI.1951-19.2019

728 Jones SR, Gainetdinov RR, Jaber M, Giros B, Wightman RM, Caron MG. 1998. Profound
729 neuronal plasticity in response to inactivation of the dopamine transporter. *Proc Natl Acad*
730 *Sci U S A* **95**: 4029-4034.

731 Jorgensen SH, Ejdrup AL, Lycas MD, Posselt LP, Madsen KL, Tian L, Dreyer JK, Herborg F,
732 Sorensen AT, Gether U. 2023. Behavioral encoding across timescales by region-specific
733 dopamine dynamics. *Proc Natl Acad Sci U S A* **120**: e2215230120. 10.1073/pnas.2215230120

734 Kearney PJ, Bolden NC, Kahuno E, Conklin TL, Martin GE, Lubec G, Melikian HE. 2023.
735 Presynaptic Gq-coupled receptors drive biphasic dopamine transporter trafficking that
736 modulates dopamine clearance and motor function. *J Biol Chem* **299**: 102900.
737 10.1016/j.jbc.2023.102900

738 Klaus A, Alves da Silva J, Costa RM. 2019. What, If, and When to Move: Basal Ganglia Circuits
739 and Self-Paced Action Initiation. *Annu Rev Neurosci* **42**: 459-483. 10.1146/annurev-neuro-
740 072116-031033

741 Kristensen AS, Andersen J, Jorgensen TN, Sorensen L, Eriksen J, Loland CJ, Stromgaard K,
742 Gether U. 2011. SLC6 neurotransmitter transporters: structure, function, and regulation.
743 *Pharmacol Rev* **63**: 585-640. 10.1124/pr.108.000869

744 Kuczenski R, Segal DS. 1992. Differential effects of amphetamine and dopamine uptake
745 blockers (cocaine, nomifensine) on caudate and accumbens dialysate dopamine and 3-
746 methoxytyramine. *J Pharmacol Exp Ther* **262**: 1085-1094.

747 Labouesse MA, Patriarchi T. 2021. A versatile GPCR toolkit to track in vivo neuromodulation:
748 not a one-size-fits-all sensor. *Neuropsychopharmacology* **46**: 2043-2047. 10.1038/s41386-
749 021-00982-y

750 Lee SJ, Lodder B, Chen Y, Patriarchi T, Tian L, Sabatini BL. 2020. Cell-type-specific
751 asynchronous modulation of PKA by dopamine in learning. *Nature*10.1038/s41586-020-
752 03050-5

753 Liu C, Goel P, Kaeser PS. 2021. Spatial and temporal scales of dopamine transmission. *Nat Rev*
754 *Neurosci* **22**: 345-358. 10.1038/s41583-021-00455-7

755 Liu C, Kershberg L, Wang J, Schneeberger S, Kaeser PS. 2018. Dopamine Secretion Is Mediated
756 by Sparse Active Zone-like Release Sites. *Cell* **172**: 706-718 e715. 10.1016/j.cell.2018.01.008

757 Lycas MD, Ejdrup AL, Sorensen AT, Haahr NO, Jorgensen SH, Guthrie DA, Stoier JF, Werner C,
758 Newman AH, Sauer M *et al*. 2022. Nanoscopic dopamine transporter distribution and
759 conformation are inversely regulated by excitatory drive and D2 autoreceptor activity. *Cell*
760 *Rep* **40**: 111431. 10.1016/j.celrep.2022.111431

761 Maeno H. 1982. Dopamine receptors in canine caudate nucleus. *Mol Cell Biochem* **43**: 65-80.
762 10.1007/BF00423094

763 Maisonneuve IM, Glick SD. 1992. Interactions between ibogaine and cocaine in rats: in vivo
764 microdialysis and motor behavior. *Eur J Pharmacol* **212**: 263-266. 10.1016/0014-
765 2999(92)90340-a

766 Markowitz JE, Gillis WF, Jay M, Wood J, Harris RW, Cieszkowski R, Scott R, Brann D, Koveal D,
767 Kula T *et al*. 2023. Spontaneous behaviour is structured by reinforcement without explicit
768 reward. *Nature* **614**: 108-117. 10.1038/s41586-022-05611-2

769 Matsuda W, Furuta T, Nakamura KC, Hioki H, Fujiyama F, Arai R, Kaneko T. 2009. Single
770 nigrostriatal dopaminergic neurons form widely spread and highly dense axonal arborizations
771 in the neostriatum. *J Neurosci* **29**: 444-453. 10.1523/JNEUROSCI.4029-08.2009

772 May LJ, Wightman RM. 1989. Effects of D-2 antagonists on frequency-dependent stimulated
773 dopamine overflow in nucleus accumbens and caudate-putamen. *J Neurochem* **53**: 898-906.
774 10.1111/j.1471-4159.1989.tb11789.x

775 Mohebi A, Collins VL, Berke JD. 2023. Accumbens cholinergic interneurons dynamically
776 promote dopamine release and enable motivation. *Elife* **12**10.7554/eLife.85011

777 Mohebi A, Wei W, Pelattini L, Kim K, Berke JD. 2024. Dopamine transients follow a striatal
778 gradient of reward time horizons. *Nat Neurosci* **27**: 737-746. 10.1038/s41593-023-01566-3

779 Nicholson C. 1985. Diffusion from an injected volume of a substance in brain tissue with
780 arbitrary volume fraction and tortuosity. *Brain Res* **333**: 325-329. 10.1016/0006-
781 8993(85)91586-0

782 Nicholson C. 1995. Interaction between diffusion and Michaelis-Menten uptake of dopamine
783 after iontophoresis in striatum. *Biophys J* **68**: 1699-1715. 10.1016/S0006-3495(95)80348-6

784 Nishikori K, Noshiro O, Sano K, Maeno H. 1980. Characterization, solubilization, and
785 separation of two distinct dopamine receptors in canine caudate nucleus. *J Biol Chem* **255**:
786 10909-10915.

787 Niv Y, Daw ND, Joel D, Dayan P. 2007. Tonic dopamine: opportunity costs and the control of
788 response vigor. *Psychopharmacology (Berl)* **191**: 507-520. 10.1007/s00213-006-0502-4

789 Olson L, Seiger A, Fuxe K. 1972. Heterogeneity of striatal and limbic dopamine innervation:
790 highly fluorescent islands in developing and adult rats. *Brain Res* **44**: 283-288. 10.1016/0006-
791 8993(72)90385-x

792 Paladini CA, Robinson S, Morikawa H, Williams JT, Palmiter RD. 2003. Dopamine controls the
793 firing pattern of dopamine neurons via a network feedback mechanism. *Proc Natl Acad Sci U*
794 *S A* **100**: 2866-2871. 10.1073/pnas.0138018100

795 Pedregosa F, Varoquaux G, Gramfort A, Michel V, Thirion B, Grisel o, Blondel M, Prettenhofer
796 P, Weiss R, Dubourg V *et al*. 2021. Scikit-learn: Machine Learning in Python. *Journal of*
797 *Machine Learning Research* **12**: 2825–2830

798 Pereira DB, Schmitz Y, Meszaros J, Merchant P, Hu G, Li S, Henke A, Lizardi-Ortiz JE, Karpowicz
799 RJ, Jr., Morgenstern TJ *et al*. 2016. Fluorescent false neurotransmitter reveals functionally
800 silent dopamine vesicle clusters in the striatum. *Nat Neurosci* **19**: 578-586. 10.1038/nn.4252

801 Pothos EN, Davila V, Sulzer D. 1998. Presynaptic recording of quanta from midbrain dopamine
802 neurons and modulation of the quantal size. *J Neurosci* **18**: 4106-4118.
803 10.1523/JNEUROSCI.18-11-04106.1998

804 Rahbek-Clemmensen T, Lycas MD, Erlendsson S, Eriksen J, Apuschkin M, Vilhardt F, Jorgensen
805 TN, Hansen FH, Gether U. 2017. Super-resolution microscopy reveals functional organization
806 of dopamine transporters into cholesterol and neuronal activity-dependent nanodomains.
807 *Nat Commun* **8**: 740. 10.1038/s41467-017-00790-3

808 Rice ME, Nicholson C. 1991. Diffusion characteristics and extracellular volume fraction during
809 normoxia and hypoxia in slices of rat neostriatum. *J Neurophysiol* **65**: 264-272.
810 10.1152/jn.1991.65.2.264

811 Richards TL, Zahniser NR. 2009. Rapid substrate-induced down-regulation in function and
812 surface localization of dopamine transporters: rat dorsal striatum versus nucleus accumbens.
813 *J Neurochem* **108**: 1575-1584. 10.1111/j.1471-4159.2009.05910.x

814 Salinas AG, Lee JO, Augustin SM, Zhang S, Patriarchi T, Tian L, Morales M, Mateo Y, Lovinger
815 DM. 2023. Distinct sub-second dopamine signaling in dorsolateral striatum measured by a
816 genetically-encoded fluorescent sensor. *Nat Commun* **14**: 5915. 10.1038/s41467-023-41581-
817 3

818 Sano K, Noshiro O, Katsuda K, Nishikori K, Maeno H. 1979. Dopamine receptors and
819 dopamine-sensitive adenylate cyclase in canine caudate nucleus. Characterization and
820 solubilization. *Biochem Pharmacol* **28**: 3617-3627. 10.1016/0006-2952(79)90408-8

821 Schultz W. 2007. Multiple dopamine functions at different time courses. *Annu Rev Neurosci*
822 **30**: 259-288. 10.1146/annurev.neuro.28.061604.135722

823 Shen HW, Hagino Y, Kobayashi H, Shinohara-Tanaka K, Ikeda K, Yamamoto H, Yamamoto T,
824 Lesch KP, Murphy DL, Hall FS *et al*. 2004. Regional differences in extracellular dopamine and
825 serotonin assessed by in vivo microdialysis in mice lacking dopamine and/or serotonin
826 transporters. *Neuropsychopharmacology* **29**: 1790-1799. 10.1038/sj.npp.1300476

827 Silm K, Yang J, Marcott PF, Asensio CS, Eriksen J, Guthrie DA, Newman AH, Ford CP, Edwards
828 RH. 2019. Synaptic Vesicle Recycling Pathway Determines Neurotransmitter Content and
829 Release Properties. *Neuron* **102**: 786-800 e785. 10.1016/j.neuron.2019.03.031

830 Sippy T, Tritsch NX. 2023. Unraveling the dynamics of dopamine release and its actions on
831 target cells. *Trends Neurosci* **46**: 228-239. 10.1016/j.tins.2022.12.005

832 Sorensen G, Rickhag M, Leo D, Lycas MD, Ridderstrom PH, Weikop P, Lilja JH, Rifes P, Herborg
833 F, Woldbye D *et al*. 2021. Disruption of the PDZ domain-binding motif of the dopamine
834 transporter uniquely alters nanoscale distribution, dopamine homeostasis, and reward
835 motivation. *J Biol Chem* **297**: 101361. 10.1016/j.jbc.2021.101361

836 Stuber GD, Hnasko TS, Britt JP, Edwards RH, Bonci A. 2010. Dopaminergic terminals in the
837 nucleus accumbens but not the dorsal striatum corelease glutamate. *J Neurosci* **30**: 8229-
838 8233. 10.1523/JNEUROSCI.1754-10.2010

839 Staal RG, Mosharov EV, Sulzer D. 2004. Dopamine neurons release transmitter via a flickering
840 fusion pore. *Nat Neurosci* **7**: 341-346. 10.1038/nn1205

841 Sulzer D, Cragg SJ, Rice ME. 2016. Striatal dopamine neurotransmission: regulation of release
842 and uptake. *Basal Ganglia* **6**: 123-148. 10.1016/j.baga.2016.02.001

843 Sulzer D, Pothos EN. 2000. Regulation of quantal size by presynaptic mechanisms. *Rev*
844 *Neurosci* **11**: 159-212. 10.1515/revneuro.2000.11.2-3.159

845 Tennyson VM, Heikkila R, Mytilineou C, Cote L, Cohen G. 1974. 5-Hydroxydopamine 'tagged'
846 neuronal boutons in rabbit neostriatum: interrelationship between vesicles and axonal
847 membrane. *Brain Res* **82**: 341-348. 10.1016/0006-8993(74)90617-9

848 Threlfell S, Clements MA, Khodai T, Pienaar IS, Exley R, Wess J, Cragg SJ. 2010. Striatal
849 muscarinic receptors promote activity dependence of dopamine transmission via distinct
850 receptor subtypes on cholinergic interneurons in ventral versus dorsal striatum. *J Neurosci*
851 **30**: 3398-3408. 10.1523/JNEUROSCI.5620-09.2010

852 Venton BJ, Troyer KP, Wightman RM. 2002. Response times of carbon fiber microelectrodes
853 to dynamic changes in catecholamine concentration. *Anal Chem* **74**: 539-546.
854 10.1021/ac010819a

855 Venton BJ, Zhang H, Garris PA, Phillips PE, Sulzer D, Wightman RM. 2003. Real-time decoding
856 of dopamine concentration changes in the caudate-putamen during tonic and phasic firing. *J*
857 *Neurochem* **87**: 1284-1295. 10.1046/j.1471-4159.2003.02109.x

858 Wiencke K, Horstmann A, Mathar D, Villringer A, Neumann J. 2020. Dopamine release,
859 diffusion and uptake: A computational model for synaptic and volume transmission. *PLoS*
860 *Comput Biol* **16**: e1008410. 10.1371/journal.pcbi.1008410

861 Wu Q, Reith ME, Kuhar MJ, Carroll FI, Garris PA. 2001. Preferential increases in nucleus
862 accumbens dopamine after systemic cocaine administration are caused by unique
863 characteristics of dopamine neurotransmission. *J Neurosci* **21**: 6338-6347.
864 10.1523/JNEUROSCI.21-16-06338.2001

865 Xie K, Wang N, Lin X, Wang Z, Zhao X, Fang P, Yue H, Kim J, Luo J, Cui S *et al*. 2020. Organic
866 electrochemical transistor arrays for real-time mapping of evoked neurotransmitter release
867 in vivo. *Elife* **9**10.7554/eLife.50345

868 Zhu S, Zhao C, Wu Y, Yang Q, Shao A, Wang T, Wu J, Yin Y, Li Y, Hou J *et al*. 2015. Identification
869 of a Vav2-dependent mechanism for GDNF/Ret control of mesolimbic DAT trafficking. *Nat*
870 *Neurosci* **18**: 1084-1093. 10.1038/nn.4060
871

872 **Table 1. List of variables used in simulation of the dorsal striatum.**

873

Variable	Abbreviation	Value	Reference
Firing rate		4 Hz	*(Paladini et al, 2003)*
Release probability		6%	*(Dreyer et al., 2010)*
DA molecules per vesicle		3000	*(Klaus et al., 2019)*
Diffusion coefficient		763 $\mu m^2 s^{-1}$	*(Nicholson, 1995)*
Tortuosity		1.54	*(Rice & Nicholson, 1991)*
Vmax		6.0 $\mu m\ s^{-1}$	See Table S2
Km		210 nM	*(Hovde et al., 2019)*
Active terminal density	-	0.04 μm^{-3}	*(Liu et al., 2021)*
Extracellular volume fraction		0.21	*(Rice & Nicholson, 1991)*
Number of neurons in simulation space	-	150	*(Matsuda et al., 2009)*

874

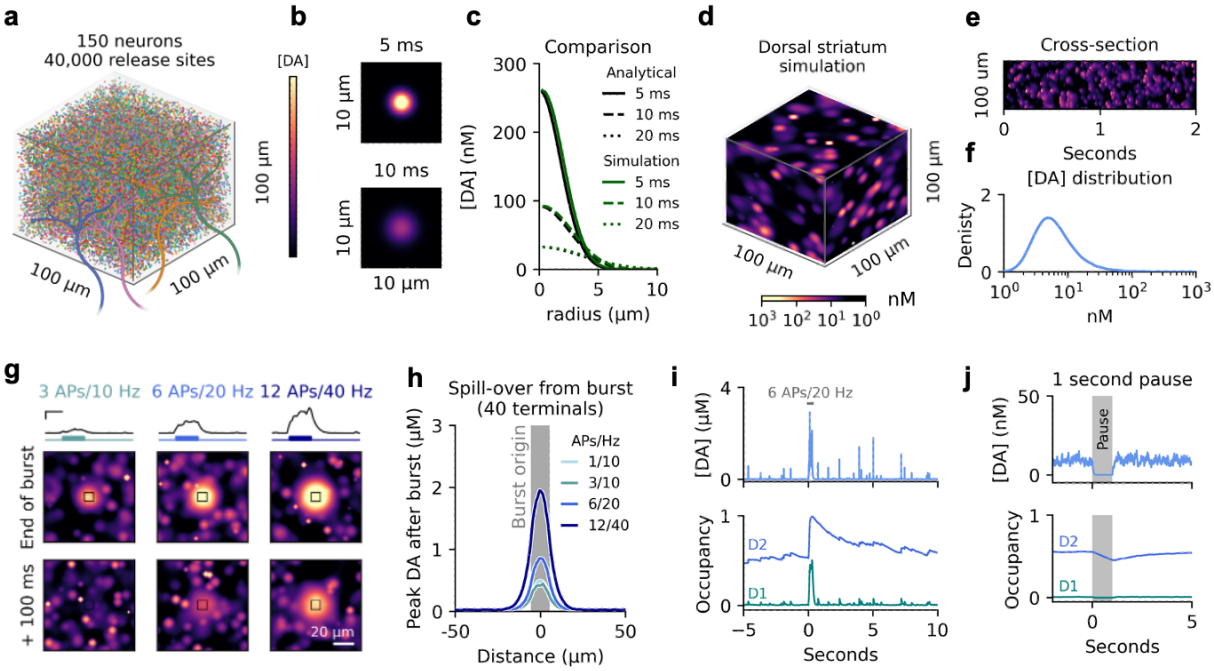

Figure 1. Large-scale 3D model of the dorsal striatum. (**a**) Self-enveloped simulation space of 100^3 µm^3 with approximately 40.000 release sites from 150 neurons. Colours of individual release sites are not matched to neurons. (**b**) Simulation of a single release event after 5 ms and 10 ms. Colour-coded by DA concentration. (**c**) Comparison of analytical solution and simulation of diffusion after a single release event at three different time points. **(d**) Representative snapshot of steady state DA dynamics at 4 Hz tonic firing with parameters mirroring the dorsal striatum. (**e**) Cross-section of temporal dynamics for data shown in (d). (**f**) Histogram of DA concentrations ([DA]) across the entire space in (d). (**g**) DA release during three burst activity scenarios for all release sites in a 10x10x10 µm cube (black boxes) and spill-over into the surrounding space. Burst simulated as increase in firing rate on top of continued tonic firing of the surrounding space. Traces on top are average DA concentrations for the marked cubes, with bursts schematized by coloured lines below. First image row is at the end of the burst, second row another 100 ms after. Scale bars for traces are 200 ms and 500 nM. Scale bar for the images is 20 µm. (**h**) Peak DA concentration reached at different distances from area with phasic activity for the three firing scenarios. (**i**) Top: representative [DA] trace 1 µm away from a release site during pacemaker and burst activity. Bottom: Occupancy of D1Rs and D2Rs for same site. (**j**) Effect of complete pause in firing for 1 second on both average [DA] and D1R and D2R occupation.

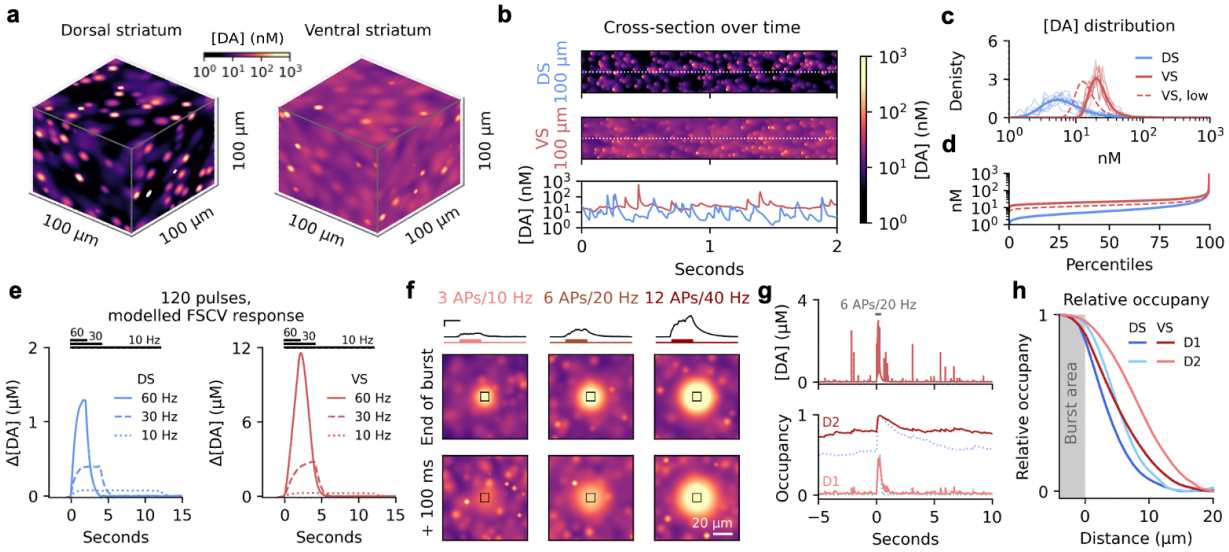

Figure 2. Regional difference in uptake greatly impact DA dynamics. (**a**) Representative snapshots of steady state dynamics at 4 Hz tonic firing with parameters mirroring the dorsal (left) and ventral striatum (right). (**b**) Cross-section of temporal dynamics for data shown in a. Bottom row show concentrations of the dashed lines in the top panels. (**c**) Normalized density of DA concentration of simulations in (a). Thick lines are for the entire space, thin lines are across time for five randomly sampled locations. Dashed red line is for simulation of the ventral striatum with lowest reported innervation density in the literature. (**d**) Same data as in (c), but for concentration percentiles. Note that even the lowest percentiles of VS were above 10 nM in [DA]. (**e**) Convoluted model response (Figure S1c) to mimic FSCV measurements mirroring the experimentally tested stimulation paradigm in *(May & Wightman, 1989)* for the dorsal (left) and ventral striatum (right) (**f**) DA release during three burst activity scenarios for all release sites in a 10x10x10 µm cube (black boxes) and spill-over into the surrounding space. Burst simulated as increase in firing rate on top of continued tonic firing of the surrounding space. Traces on top are average DA concentrations for the marked cubes, with bursts schematized by coloured lines below. First image row is at the end of the burst, second row another 100 ms after. Scale bars for traces are 200 ms and 500 nM. Scale bar for the images is 20 µm. (**g**) Top: representative [DA] trace 1 µm away from a release site during pacemaker and burst activity. Bottom: Occupancy of D1Rs and D2Rs for same site. Occupancy data from corresponding DS simulation on Figure 1k shown in as dotted line. (**h**) Peak occupancy at different distances from the area bursting normalized to maximal and minimum occupancy.

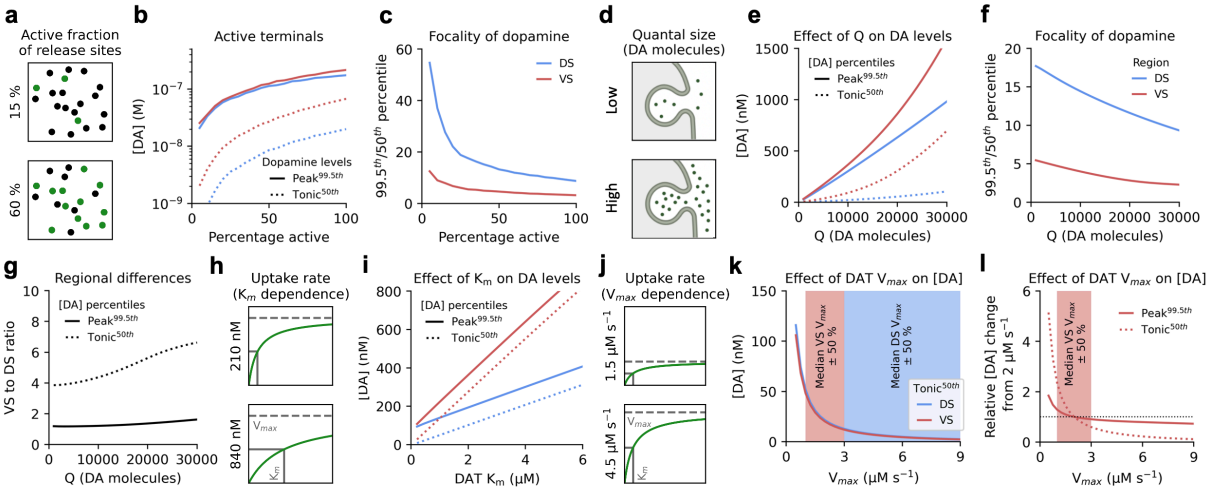

Figure 3. Sensitivity of the model to parameter changes. (**a**) Schematic of the fraction of active release sites. Black dots are inactive sites and green dots indicate actively releasing sites. (**b**) Effect of changing fraction of active release sites on DA concentrations. Blue line, DS peak DA concentration (99.5th percentile); Red line, VS peak DA concentration (99.5th percentile); Dotted blue line, DS tonic DA concentration (50th percentile); Dotted red line, VS tonic DA concentration (50th percentile). (**c**) Ratio between peak (99.5th percentile) and tonic (50th percentile) concentrations across fractions of active release sites in the DS (blue line) and VS (red line) as a measure of DA signal focality. (**d**) Schematic of changing quantal size (Q). (**e**) Effect of changing quantal size on tonic and peak DA concentrations in DS (blue lines) and VS (red lines). (**f**) Ratio between peak and tonic concentrations across various quantal sizes in in DS (blue line) and VS (red line). (**g**) Relative difference between the DS and VS for peak (black line) and tonic DA (dotted line) at different quantal sizes. (**h**) Schematic of changing DAT K_m. (**i**) Effect of changing DAT K_m on DA concentrations in DS (blue lines) and VS (red lines). **j,** Schematic of changing DAT V_{max}. (**k**) Effect of changing DAT V_{max} on DA concentrations. Shaded areas are median V_{max} of the two regions (DS and VS) as found in the literature shown in Table S2 ± 50%. (**l**) Effect of changing DAT V_{max}, with tonic (50th percentile) and peak (99.5th percentile) DA concentrations normalized to their value at 2 µm s^{-1} (median value for VS). Shaded area indicates median V_{max} for VS found in the literature shown in Table S2 ± 50%.

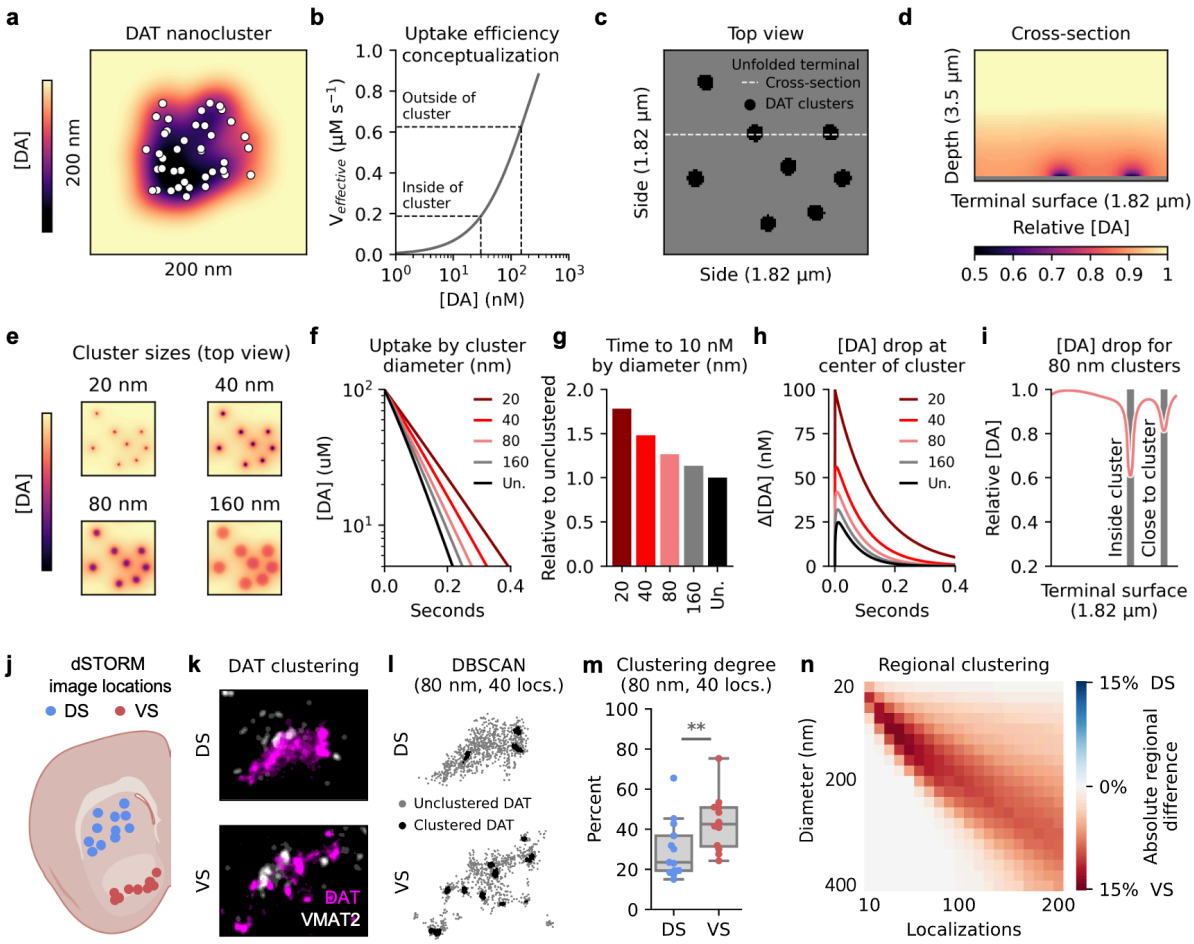

Figure 4. DAT nanoclustering reduces uptake and shows regional variation. (**a**) Schematic of dense DA cluster. White dots represent individual DAT molecules, and colour gradient the surrounding DA concentration. (**b**) Effective transport rate dependent on local concentration. (**c**) Top view of unfolded DA varicosity. Black shapes denote clusters of DAT. Dashed white line indicates placement of cross-section shown in (d). (**d**) Cross section showing DA concentration in space surrounding varicosity unfolded in c. Grey line at the bottom is surface of the varicosity. Colour-coded for DA concentration. (**e**) Top view from (c), but colour coded for DA concentration immediately above membrane surface at different DAT cluster sizes. (**f**) Mean [DA] over time for different DAT cluster sizes and unclustered (Un.). (**g**) Time to reach a mean DA concentration of 10 nM for different DAT cluster sizes and unclustered (Un.). (**h**) Difference between DA concentration at the centre of clusters and mean concentration throughout the simulation for different cluster sizes and unclustered (Un.). (**i**) Concentrations across a cross section of a surface with 80 nm diameter clusters. Shaded areas highlight cluster locations. (**j**) Location of images of the dorsal (DS) and ventral striatum (VS) in striatal slices from mice as imaged in *(Sorensen et al., 2021)* with direct stochastic optical reconstruction microscopy (dSTORM). (**k**) Two representative DA varicosities from DS and VS with VMAT2 in white and DAT in magenta. Images are 1.5x2 μm. (**l**) Individual DAT localizations from images in (k) coloured by clustering. Black indicates localization identified as clustered based on DBSCAN with parameters 80 nm diameter and 40 localizations. Grey indicates unclustered localizations. (**m**) Quantification of clustering across all images in (j) with parameters in (l). Welch's two-sample t-test, P = 0.012(*), n = 12 (DS) and 13 (VS). (**n**) Absolute difference in percentage of clustering as assessed with

DBSCAN across a range of parameters. VS has a higher propensity to cluster across cluster sizes typically reported for DAT clusters.